APL Materials

Tetragonal Mn_3Sn Heusler films with large perpendicular magnetic anisotropy deposited on metallic MnN underlayers using amorphous substrates

Cite as: APL Mater. **7**, 031103 (2019); https://doi.org/10.1063/1.5066594
Submitted: 16 October 2018 . Accepted: 09 February 2019 . Published Online: 07 March 2019

Yari Ferrante, Jaewoo Jeong, Rana Saha, Sergey V. Faleev, Mahesh G. Samant, Teya Topuria, Hakan Deniz, and Stuart S. P. Parkin

ARTICLES YOU MAY BE INTERESTED IN

Anomalous Hall effect in thin films of the Weyl antiferromagnet Mn_3Sn
Applied Physics Letters **113**, 202402 (2018); https://doi.org/10.1063/1.5064697

Anomalous Hall effect in polycrystalline Mn_3Sn thin films
Applied Physics Letters **113**, 222405 (2018); https://doi.org/10.1063/1.5051495

Magnetic phase dependence of the anomalous Hall effect in Mn_3Sn single crystals
Applied Physics Letters **112**, 132406 (2018); https://doi.org/10.1063/1.5021133

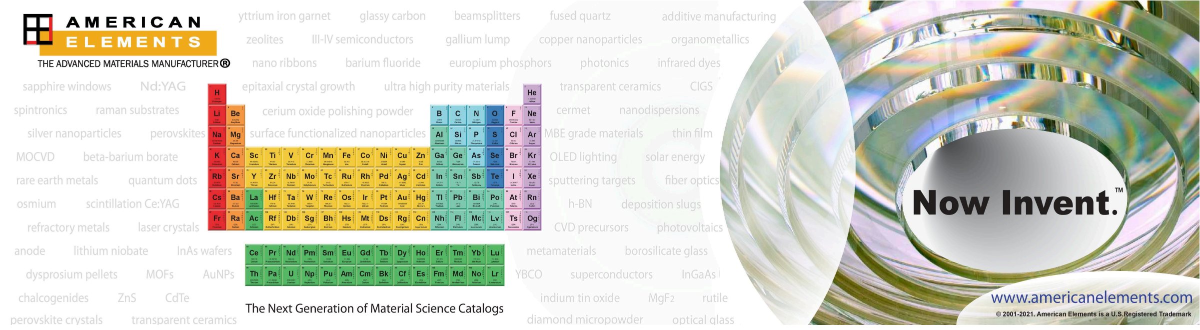

© 2019 Author(s).

Tetragonal Mn_3Sn Heusler films with large perpendicular magnetic anisotropy deposited on metallic MnN underlayers using amorphous substrates

Cite as: APL Mater. **7**, 031103 (2019); doi: 10.1063/1.5066594
Submitted: 16 October 2018 • Accepted: 9 February 2019 •
Published Online: 7 March 2019

Yari Ferrante,[1] Jaewoo Jeong,[1,2] Rana Saha,[3] Sergey V. Faleev,[3] Mahesh G. Samant,[1] Teya Topuria,[1] Hakan Deniz,[3] and Stuart S. P. Parkin[1,3,a)]

AFFILIATIONS

[1] IBM Research—Almaden, San Jose, California 95120, USA
[2] New Memory Technology Lab, Semiconductor R&D Center, Samsung Electronics, Milpitas, California 95053, USA
[3] Max-Planck Institute for Microstructure Physics, 06120 Halle (Saale), Germany

[a)] **Author to whom correspondence should be addressed:** stuart.parkin@mpi-halle.mpg.de

ABSTRACT

Tetragonal Heusler compounds that exhibit large perpendicular magnetic anisotropy are promising materials for advanced spintronic devices. A prerequisite are thin films whose tetragonal axis is oriented perpendicular to the plane of the films. Here we show that highly textured, (001) oriented, tetragonal Mn_3Sn layers can be prepared using metallic zinc-blende (ZB) MnN as underlayers. Moreover, we show that these layers can be deposited on amorphous substrates using reactive magnetron sputtering. The ferrimagnetic Mn_3Sn layers exhibit perpendicularly magnetized hysteresis loops with coercive fields of ~2 T. Stoichiometric ZB-MnN underlayers share an "equivalent" Mn-Mn layer at the interface with Mn_3Sn, thus promoting their oriented growth. Other nitride underlayers are not effective due to their rock-salt (RS) crystal structure and the absence of Mn. Density functional theory calculations confirm that tetragonal Mn_3Sn Heusler films are energetically stable when interfaced with ZB-MnN underlayers and not with any of the other RS nitride underlayers considered here. Such Heusler compounds have much promise as electrodes for magnetic tunnel junction memory elements for deeply scaled magnetic random access memories.

© 2019 Author(s). All article content, except where otherwise noted, is licensed under a Creative Commons Attribution (CC BY) license (http://creativecommons.org/licenses/by/4.0/). https://doi.org/10.1063/1.5066594

Magnetic materials displaying large *volume* perpendicular magnetic anisotropy (PMA) at room temperature (RT) are of significant interest for magnetic disk drive and rare-earth free hard magnet applications as well as for advanced spintronic applications such as the magnetic electrodes in magnetic tunnel junction (MTJ) devices. MTJs are used as the memory elements in deeply scaled spin transfer torque (STT) magnetic random access memories (STT-MRAM).[1,2] Within an STT-MRAM architecture, each MTJ device is placed between two conducting wires—an upper wire and a lower wire—that are generally made of amorphous or polycrystalline materials. These layers are utilized to flow currents through the MTJ to read their resistance state and to write them by exploiting the STT mechanism.[3,4] For this latter purpose, the magnetic films that form the MTJ, e.g., magnetic Heusler compounds, must be deposited on metallic underlayers having an appropriate crystal structure and texture to promote the crystal orientation needed for Heusler films with PMA. Within the large family of Heusler alloys,[5] Mn-based tetragonal compounds[6,7] are of particular interest. Thin (001)-oriented films formed from the binary Mn_3Z (Z = Ga, Ge, Sb, Sn) Heusler materials[8–12] possess large uniaxial PMA stemming from bulk magnetocrystalline anisotropy. The "broken" symmetry of the tetragonal structure,[13] composed of alternating Mn-Mn and Mn-Z

© Author(s) 2019

atomic layers, inherently promotes the alignment of the Mn magnetic moments along the elongated *c* axis, which is perpendicular to the basal plane of the Mn_3Z unit cell (Fig. S1 of the supplementary material).

In prior work,[11] we reported the use of TaN/$IrMn_3$ and TaN/$IrMn_3$/TaN as suitable underlayers for the growth of Heusler-based perpendicular MTJ devices on amorphous or polycrystalline materials. However, annealing these devices above some characteristic temperature results in diffusion of Ir from the $IrMn_3$ layer into the Heusler compound, degrading its magnetic properties. Iridium is heavy and gives rise to significant spin-orbit-coupling-derived damping that deteriorates the performance of the MTJ device. Other underlayer materials that are known for promoting the oriented growth of tetragonal Mn-based Heusler films are (face-centered cubic) *fcc*-Pt (Refs. 14 and 15), (body-centered cubic) *bcc*-Cr (Refs. 10, 11, and 16), and -CoX (X = Al, Ga, Ge, Sn) layers (with a B2 structure).[12] However, these underlayers are typically grown on MgO(001) single crystalline substrates. Note that Cr and the CoX compounds are formed from light elements that give rise to significantly less damping than Ta, Ir, or Pt. Nevertheless, these layers are not compatible with CMOS applications in which amorphous or polycrystalline underlayers are generally used. Therefore, what is needed is a thermally stable (001)-textured metallic underlayer on amorphous Si(001)/SiO_2 substrates, containing only light elements and preferably Mn, and that promotes the growth of Mn-based tetragonal Heusler films with the required (001) crystal orientation.

MnN is a metallic compound that was theoretically predicted to have a zinc-blende (ZB) cubic structure as its lowest energy configuration.[17–19] However, to date, only the tetragonally distorted rock-salt (t-RS) structure of MnN (t-RS-MnN) has been found experimentally.[20–22] The in-plane lattice mismatch (~6%) between t-RS-MnN (with in-plane lattice constant a[t-RS-MnN] ~ 4.17 Å) and a tetragonal Mn_3Sn (t-Mn_3Sn) Heusler compound (a[t-Mn_3Sn] ~ 3.93 Å) is smaller than that between ZB-MnN (a[ZB-MnN] ~ 4.30 Å) and t-Mn_3Sn (~9%). Nevertheless, the atomic configuration of the ZB structure of MnN is preferable over its RS (or t-RS) structure since it allows the sharing of an "equivalent" Mn-Mn layer at the interface with t-Mn_3Sn (Fig. 1), thus promoting the (001)-oriented growth and, consequently, PMA of the Heusler layer.

In this work, we demonstrate that stoichiometric and metallic MnN thin underlayers with a ZB crystal structure can be grown by reactive magnetron sputtering at ambient temperature and satisfy the aforesaid requirements. We demonstrate that ZB-MnN is preferred over three other well-known RS-XN underlayers that we explore (X = Ti, V, and Ta), all deposited under similar conditions on amorphous substrates. MnN is the only one [despite its larger in-plane lattice mismatch with Mn_3Sn as compared to RS-TiN and RS-VN (7.5% and 4.6%, respectively) with Mn_3Sn] that displays a strong (001)-texture (regardless of the underlayer it is deposited onto) and promotes the growth of tetragonal Mn_3Sn thin films which show large PMA at RT with coercive fields >1 T. Density functional theory calculations confirm that a system formed by a ZB-MnN underlayer and a tetragonal Mn_3Sn Heusler layer is energetically more stable

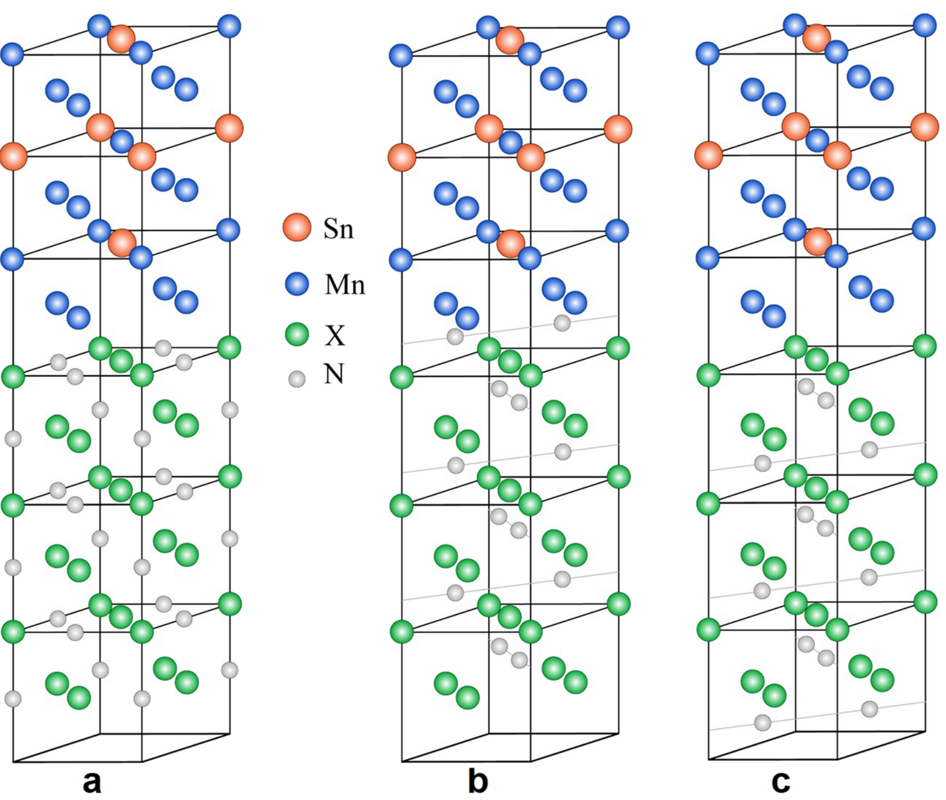

FIG. 1. Schematics of the Mn_3Sn/XN systems formed by three Mn_3Sn formula units with Mn-Mn terminations interfacing (a) a RS-XN underlayer, (b) a ZB-XN underlayer with a "buckled N" termination, and (c) a ZB-XN underlayer with a "N is not buckled" termination. Note that the only difference between these three structures is the position of the N atoms. Atom sizes are not to scale.

© Author(s) 2019

than the combination of any RS-nitride underlayer (studied here) and t-Mn_3Sn, thus supporting our experimental findings.

The goal of the theoretical calculations in this paper is to determine the stability of a thin film of a tetragonal Mn_3Sn Heusler deposited on a XN underlayer, with X = Ti, V, and Mn [note that TaN is not considered here because the deposited TaN underlayers do not display the relevant (001) crystal orientation]. As a first step to determine this stability, we find the crystal and magnetic structures of the lowest energy configurations of bulk TiN, VN, and MnN by performing density functional theory (DFT) calculations using the VASP program (see more details in the supplementary material). For each of these three materials, we investigate the ZB and RS structures for both cubic and tetragonally distorted lattices, with different magnetic configurations [non-magnetic (NM), ferromagnetic (FM), and different antiferromagnetic (AFM) configurations of the initial magnetic moments on the Ti, V, and Mn atoms].

The lowest energy configuration of TiN is found to be the NM cubic RS structure with lattice constant a[RS-TiN] = 4.25 Å. This lattice constant agrees very well with a previously found theoretical value of a[RS-TiN] = 4.255 Å (Ref. 23) and an experimental value of a[RS-TiN] = 4.24 Å (Ref. 24). The lowest energy magnetic configuration of the ZB-TiN is also NM, and it is 0.6 eV (per formula unit) higher in energy than the ground state RS-TiN configuration.

The lowest energy configuration of VN is found to be the AFM cubic RS structure with lattice constant a[RS-VN] = 4.12 Å. V atoms in the lowest energy configuration have a small magnetic moment of $0.3\mu_B$ and $-0.3\mu_B$ alternating along the [001] direction (the total magnetic moment of the system is zero). The calculated lattice constant agrees very well with the experimental values of a[RS-VN] = 4.13–4.14 Å (Refs. 25–27). Note that the AFM RS structure is only 0.005 eV lower in energy as compared to the NM RS structure with the same lattice constant. The lowest energy configuration of ZB-VN is also AFM, and it is 0.25 eV (per formula unit) higher in energy than the RS-VN ground state configuration.

The lowest energy configuration of MnN is rather determined to be the AFM cubic ZB structure with lattice constant a[ZB-MnN] = 4.30 Å. Mn atoms in the lowest energy configuration possess a magnetic moment of $1.5\mu_B$ and $-1.5\mu_B$ alternating along the [001] direction (the total magnetic moment of the system is zero). The obtained lattice constant is in the middle of a range of previously found theoretical values for an AFM ZB-MnN: a[ZB-MnN] = 4.31 Å (Ref. 17), a[ZB-MnN] = 4.376 Å (Ref. 28), and a[ZB-MnN] = 4.22 Å (Ref. 18). The lowest energy configuration of a RS-MnN is the tetragonally distorted (t-RS) AFM system with in-plane and out-of-plane lattice constants a[t-RS-MnN] = 4.17 Å and c[t-RS-MnN] = 4.107 Å (note that this configuration is only 0.004 eV lower in energy as compared to the cubic RS configuration with a[RS-MnN] = 4.15 Å). The Mn atoms in the t-RS structure have a magnetic moment of $3.0\mu_B$ and $-3.0\mu_B$ alternating along the [001] direction (the total magnetic moment of the system is zero). The t-RS configuration of MnN is 0.16 eV (per formula unit) higher in energy than the ZB-MnN ground state configuration. The lattice constants of t-RS-MnN that we find are in good agreement (within 2%) with previous predictions, a[t-RS-MnN] = 4.18 Å and c[t-RS-MnN] = 4.04 Å (Ref. 17), and experimental results, a[t-RS-MnN] = 4.256 Å and c[t-RS-MnN] = 4.189 Å (Ref. 29).

Our finding that the ZB structure of MnN represents the lowest total energy configuration agrees with previous theoretical calculations.[17–19] On the other hand, only the t-RS structure has been observed experimentally so far.[20,21] Miao and Lambrecht[19] attributed the experimental observation of the stable t-RS-MnN structure to the possible presence of nitrogen vacancies in the samples, claiming that as little as 4% of nitrogen vacancies is enough to stabilize the RS structure over the ZB one.

Recently, we determined (using similar VASP calculations) the bulk crystal and magnetic structure of the Mn_3Sn Heusler compound, showing that it possesses volume PMA.[7] The lowest energy configuration of Mn_3Sn was found to be the $D0_{22}$ tetragonal structure with in-plane and out-of-plane lattice constants a[t-Mn_3Sn] = 3.93 Å and c[t-Mn_3Sn] = 7.47 Å, respectively. The magnetic moment of the Mn atoms within the Mn-Sn *xy*-plane is AFM coupled with the magnetic moment of the two Mn atoms within the Mn-Mn *xy*-plane of Mn_3Sn, resulting in a ferrimagnetic configuration (Fig. S1 of the supplementary material).

In order to evaluate the stability of a Mn_3Sn Heusler thin film deposited onto a XN underlayer, we calculate the work of adhesion, W_{AD}, of a $Mn_3Sn(001)$ slab onto a XN(001) underlayer. The work of adhesion is defined as the energy required to separate a Mn_3Sn/XN system into two free surfaces,

$$W_{AD} = E[Mn_3Sn(001)] + E[XN(001)] - E[Mn_3Sn(001)/XN(001)]. \quad (1)$$

Here $E[Mn_3Sn(001)/XN(001)]$ is the total energy of the studied interface (slabs of Mn_3Sn/XN/vacuum), $E[Mn_3Sn(001)]$ is the total energy of a free $Mn_3Sn(001)$ surface (slabs of Mn_3Sn/vacuum), and E[XN(001)] is the total energy of a free XN(001) surface (slabs of XN/vacuum). The attractive interaction between two surfaces corresponds to a positive W_{AD}. The Mn_3Sn slab is modeled with three formula units of Mn_3Sn stacked along the (001) direction (each formula unit includes two *xy*-planes—one plane with two Mn atoms and the other with one Mn and one Sn atom). The RS-XN slab is modeled with six XN layers stacked along the (001) direction (one layer of RS-XN includes two X atoms and two corresponding N atoms), as shown in Fig. 1(a). We conduct the calculations for four different types of XN underlayers: RS-TiN, RS-VN, t-RS-MnN, and ZB-MnN. The geometry used for modeling all the $Mn_3Sn(001)$/XN(001) interfaces can be visualized (Fig. 1) as the "backbone" *fcc* structure (slightly compressed along the z-direction on the Mn_3Sn side of the interface), which consists of Mn and Sn atoms on the Mn_3Sn side and X atoms on the XN side (N atoms are not part of this "backbone" *fcc* structure). The calculations of the $Mn_3Sn(001)$/XN(001) system are performed with two possible terminations of Mn_3Sn at the interface: Mn-Mn and Mn-Sn terminations. The simulation cell for a $Mn_3Sn(001)$/XN(001) interface with Mn-Mn-terminated Mn_3Sn and the RS-XN is shown in Fig. 1(a). For the ZB structure of XN with X = Mn, the calculations are performed for two possible terminations of XN: one termination with N atoms [called "buckled N" termination, Fig. 1(b)] and the other termination with X atoms [called "N is not buckled" termination, Fig. 1(c)]. Note that the simulation cells also contain the vacuum layer that is not illustrated in Fig. 1.

For all these Mn_3Sn/XN systems, the configuration with the Mn-Mn-termination of Mn_3Sn is found to have the lowest total energy. For the ZB-MnN substrate, the "buckled N" termination [Fig. 1(b)] has the lowest total energy. For the Mn_3Sn/MnN systems,

© Author(s) 2019

TABLE I. In-plane lattice constant, a = a[XN], work of adhesion, W_{AD}, and final work of separation, W_{FIN}, of the Mn_3Sn/XN systems for the four considered XN substrates.

Interface	a (Å)	W_{AD} (eV)	W_{FIN} (eV)
Mn_3Sn/RS-TiN	4.25	3.26	−1.02
Mn_3Sn/RS-VN	4.12	3.41	−0.31
Mn_3Sn/t-RS-MnN	4.17	3.67	−0.26
Mn_3Sn/ZB-MnN	4.30	5.00	0.57

irrespective of the MnN structure, the lowest total energy configuration is achieved with the Mn atoms at the interface coupling antiferromagnetically to each other. The results of these calculations are summarized in Table I. The interactions between the Mn_3Sn and XN surfaces are attractive (W_{AD} is positive) for all cases considered here. In the cases of RS-XN (or t-RS), W_{AD} varies in the range 3.26-3.67 eV, whilst it is significantly larger (W_{AD} = 5.00 eV) for the ZB-MnN case, indicating that the adhesion of a Mn_3Sn Heusler film to a ZB-MnN underlayer is expected to be significantly stronger.

W_{AD}, obtained by considering the same fixed in-plane lattice constant of the XN underlayer, a = a[XN], for all surfaces—Mn_3Sn(001)/XN(001)/vacuum, Mn_3Sn(001)/vacuum, and XN(001)/vacuum—provides a useful estimate of the energy barrier that needs to be overcome during the initial separation (i.e., Mn_3Sn still has the in-plane lattice constant a) of the Mn_3Sn thin film from the Mn_3Sn/XN interface. However, after this initial separation, the free thin film of Mn_3Sn would eventually transform into bulk t-Mn_3Sn. Thus, in the final state, the "separated" Mn_3Sn film should have its own tetragonal lattice constants (i.e., a[t-Mn_3Sn] and c[t-Mn_3Sn]). We, therefore, compute the final work of separation, W_{FIN}, needed to separate the Mn_3Sn thin film from the XN underlayer as the total energy difference between the final and initial states, in which the initial state is the Mn_3Sn/XN interface, with in-plane lattice constant a, and the final state consists of the free XN film, with the same a, and the bulk t-Mn_3Sn Heusler film with its corresponding tetragonal lattice constants,

$$W_{FIN} = 3 \times E_{bulk}[\text{t-Mn}_3\text{Sn}(001)] + E[\text{XN}(001)] - E[\text{Mn}_3\text{Sn}(001)/\text{XN}(001)]. \quad (2)$$

Here E[XN(001)] and E[Mn_3Sn(001)/XN(001)] are the same energies as in Eq. (1) and E_{bulk}[t-Mn_3Sn(001)] is the total energy of bulk tetragonal Mn_3Sn per formula unit. The factor 3 in front of E_{bulk}[t-Mn_3Sn(001)] reflects the fact that we use three formula units of Mn_3Sn for the calculation of the Mn_3Sn slab.

The estimated values of W_{FIN} are presented in Table I. Negative values of W_{FIN} for RS-TiN, RS-VN, and t-RS-MnN indicate that Mn_3Sn is predicted to be unstable when deposited on these underlayers; on the other hand, the positive value of W_{FIN} for ZB-MnN reveals that Mn_3Sn is expected to be stable on a ZB-MnN underlayer. These calculations are in good agreement with our experimental findings. The stability of a Mn_3Sn Heusler film on a ZB-MnN underlayer (which manifests itself as both the positive W_{FIN} and the largest W_{AD} among all the considered substrates) could be attributed to the fact that at the Mn_3Sn/MnN interface, formed by a Mn-Mn-terminated Mn_3Sn and a "N-buckled"-terminated ZB-MnN [Fig. 1(b)], the Mn-Mn layer of Mn_3Sn is equivalent to the last layer of ZB-MnN. Such a "continuous" transition between the Mn_3Sn and ZB-MnN structures, sharing a common Mn-Mn layer, does not occur for any other RS-XN underlayers [Fig. 1(a)]. This "continuous" transition between the Mn_3Sn and ZB-MnN structures is indeed due to the small difference between the actual d/a ratio (0.492) from the ideal value (0.500). Note that here a is the lattice constant of ZB-MnN shown in Table I and d is the distance between the Mn-Mn layer of Mn_3Sn and the Mn-Mn layer of ZB-MnN. For the Mn_3Sn/RS-XN structures with X = Ti, V, and Mn, the corresponding d/a ratios are significantly lower and 8%-10% smaller than the "ideal" continuous transition (d/a = 0.460, 0.456, and 0.447 for X = Ti, V, and Mn, respectively).

Mn_xN films are deposited by reactive magnetron sputtering in an ultra-high vacuum chamber with a base pressure of ~1×10^{-9} Torr. The Mn/N ratio is controlled by tuning the Ar:N_2 gas mixture (more details can be found in the supplementary material) and determined by Rutherford backscattering spectrometry (RBS) measurements [Fig. S2(a) of the supplementary material]. The Mn:N ratio decreases with increasing N_2 content within the sputter gas mixture; a 1:1 stoichiometric composition (hereafter referred to as MnN) was obtained for an Ar:N_2 ratio of 20:80 (by flow). The deposition rate significantly decreases with increasing N_2 content, as illustrated in Fig. S2(b) of the supplementary material. The conductivity of a MnN film is determined—using a sample with the structure Si(001)/250 Å SiO_2/50 Å Ta/3 Å CoFeB/200 Å MnN/20 Å MgO/20 Å Ta—to be ~1.42 MS/m (more details can be found in the supplementary material). Compared to other metallic underlayer materials often used in MTJ devices, MnN conductivity is ~1.7× smaller than Ti (2.38 MS/m) and ~2.5× and ~ 7× larger than Ta (0.56 MS/m) and TaN (0.2 MS/m), respectively.

To investigate its structural properties, a 200 Å thick MnN film is deposited at RT on a MgO(001) substrate using a 20 Å thick MgO buffer layer. The out-of-plane θ-2θ high-resolution X-ray diffraction (HR-XRD) scan of the sample shows that the MnN film has excellent crystallinity and (001) texture [Fig. 2(a)]. The heteroepitaxial growth of the MnN film on top of the MgO(001) substrate is confirmed by high-angle annular dark-field (HAADF) scanning transmission electron microscopy (STEM) showing a smooth and distinct interface between the layers [Fig. 2(b)]. The sample surface, measured by atomic force microscopy (AFM), is found to be very smooth with a root mean square roughness (r_{rms}) of ~2.2 Å (Fig. S3 of the supplementary material).

From Fig. 2(a), the out-of-plane c lattice parameter of MnN is extracted to be ~4.25 Å, in good agreement with our theoretical predictions for a cubic ZB-MnN structure. Meinert *et al.*[22] recently reported similar c values for MnN but with a smaller in-plane lattice constant of ~4.1 Å (i.e., tetragonal distortion along the perpendicular direction). Our c lattice parameter is bigger than the ones previously reported by Suzuki *et al.* (~4.19 Å) and Yang *et al.* (~4.12 Å) for MnN samples with in-plane lattice constants of ~4.26 Å and ~4.22 Å, respectively (i.e., tetragonal distortion along the in-plane direction).[20,21] Although here the MnN film in-plane lattice constant is not measured, we expect this to be the same as that of the RS-MgO buffer layer (4.21 Å), based on the STEM image in Fig. 2(b). In an hypothetical case, a RS-MnN film [which is predicted to have a smaller in-plane lattice parameter (4.17 Å and 4.15 Å for a t-RS and cubic RS, respectively) than the ZB structure (4.30 Å)] is expected to

© Author(s) 2019

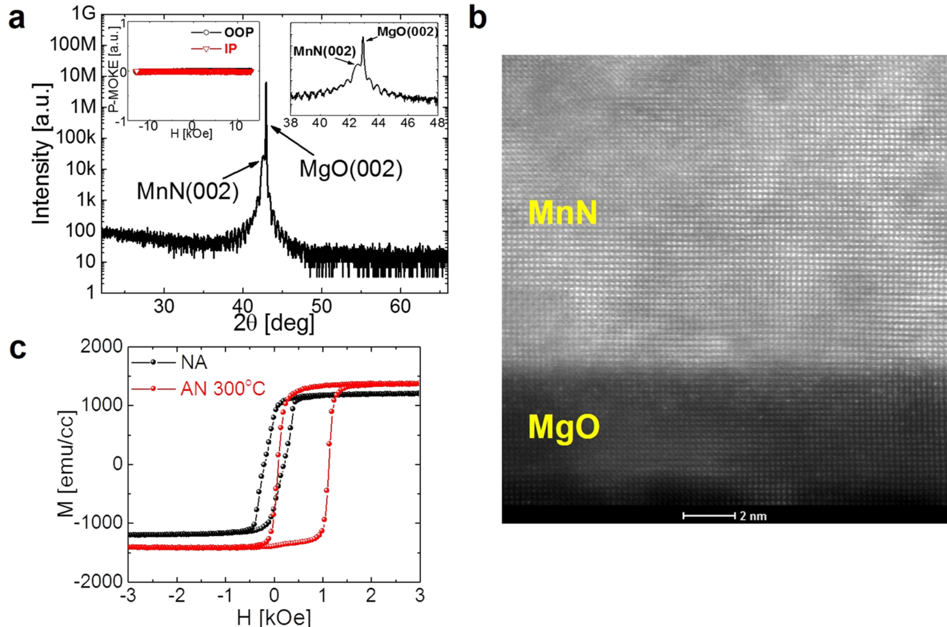

FIG. 2. (a) HR-XRD out-of-plane θ-2θ scan of a sample with the structure: MgO(001)/20 Å MgO/200 Å MnN/30 Å Ta. The inset in the top right corner is a zoomed-in view of the Bragg diffraction peaks from the MnN film and the MgO(001) substrate: the MnN thickness fringes are observed. The inset in the top left corner displays the in-plane (IP) and out-of-plane (OOP) P-MOKE measurements of the MnN film. No magnetic signal is detected for either configuration. (b) HAADF-STEM image of the sample in (a). A well-defined interface between the epitaxial MnN film and the substrate is clearly visible. The bright spots, within the MnN layer, correspond to the Mn atoms. N atoms have small atomic number and cannot be distinguished in HAADF imaging. (c) Vibrating sample magnetometry (VSM) measurements of a sample with the structure: Si(001)/250 Å SiO_2/50 Å Ta/3 Å CoFeB/300 Å MnN/20 Å CoFeB/20 Å MgO/20 Å Ta. The sample hysteresis loops are measured in the in-plane configuration, at ambient temperature, before (NA) and after being annealed at 300 °C for 30 min (AN 300 °C) in a high-vacuum furnace with a 1 T field applied parallel to the sample surface to set the in-plane exchange bias (note the 20 Å CoFeB film has in-plane magnetization). The magnetic moment of the CoFeB film after annealing increases by 15%, as the amorphous film crystallizes during annealing.

undergo a tensile strain to compensate for the in-plane lattice mismatch with MgO; as a consequence, its distorted *c* lattice parameter would be smaller than its calculated bulk value (4.107 Å and 4.15 Å for t-RS and cubic RS, respectively), and, thus, far smaller than the one we find from HR-XRD measurements (~4.25 Å). Furthermore, from the analyses of the fast Fourier transform (FFT)-filtered images obtained from HAADF micrographs of the MnN film, we estimate the in-plane and out-of-plane lattice constants to be the same, i.e., ~4.26 Å (Fig. S4 of the supplementary material), in good agreement with our theoretical and experimental data (the lattice parameter of RS-MgO is also confirmed, using similar analyses, to be ~4.21 Å). Therefore, we rule out the possibility of having formed a MnN film with a t-RS structure. Our findings represent the first experimental observation of MnN thin films having a cubic ZB structure.

Polar magneto-optical Kerr effect (P-MOKE) measurements, for both in-plane and out-of-plane geometries, of this sample establish that the MnN film has no net moment at RT [the top-left inset in Fig. 2(a)]. Moreover, we find that similarly grown MnN layers on Si(001)/SiO_2 substrates promote (after anneal) an in-plane exchange bias field when interfaced with a 20 Å thick FM CoFeB layer. As displayed in Fig. 2(c), the in-plane magnetization hysteresis loop of the annealed CoFeB layer is shifted by ~500 Oe along the H axis. These results suggest that the MnN film is rather an AFM in agreement with our theoretical predictions of ZB-MnN films.

The influence of various 100 Å thick metallic nitride underlayers—namely, MnN, TiN, VN, and TaN—on the structural and magnetic properties of an overlying 200 Å thick Mn_3Sn film is explored for two different film stack systems shown in Figs. 3(a) and 3(d). In the first case, the nitride underlayers are deposited directly on an amorphous SiO_2 surface, whilst in the latter on an oxygen-free 50 Å Ta/3 Å CoFeB amorphous bilayer. We note the 3 Å CoFeB layer is NM. XRD data in Fig. 3(b) suggest that only the ZB-MnN film has good crystallinity with a strong (001) texture when deposited directly on the amorphous SiO_2 surface. The HR-TEM image in Fig. 4(a) shows that this MnN film has very good ordering with atomic planes parallel to the sample surface in close proximity of its interface with the SiO_2 layer; thus, we expect similar properties for MnN films even thinner than 100 Å. No other distinct diffraction peaks corresponding to a different phase or orientation of MnN are detected. The ZB-MnN underlayer promotes the growth of a polycrystalline tetragonal Mn_3Sn Heusler film with the preferred (001) out-of-plane orientation. From the Mn_3Sn diffraction peaks, we determine c[t-Mn_3Sn] to be ~7.53 Å, in good agreement with our theoretical predictions. The Mn_3Sn(002) tetragonal superlattice peak is also observed, indicating the layered ordering of alternating Mn-Mn and Mn-Sn atoms [we expect similar ordering for other Mn_3-based tetragonal Heusler compounds, e.g., Mn_3Ga, Mn_3Ge, and Mn_3Sb, as they can also share a Mn-Mn termination at the interface with the ZB-MnN underlayer

© Author(s) 2019

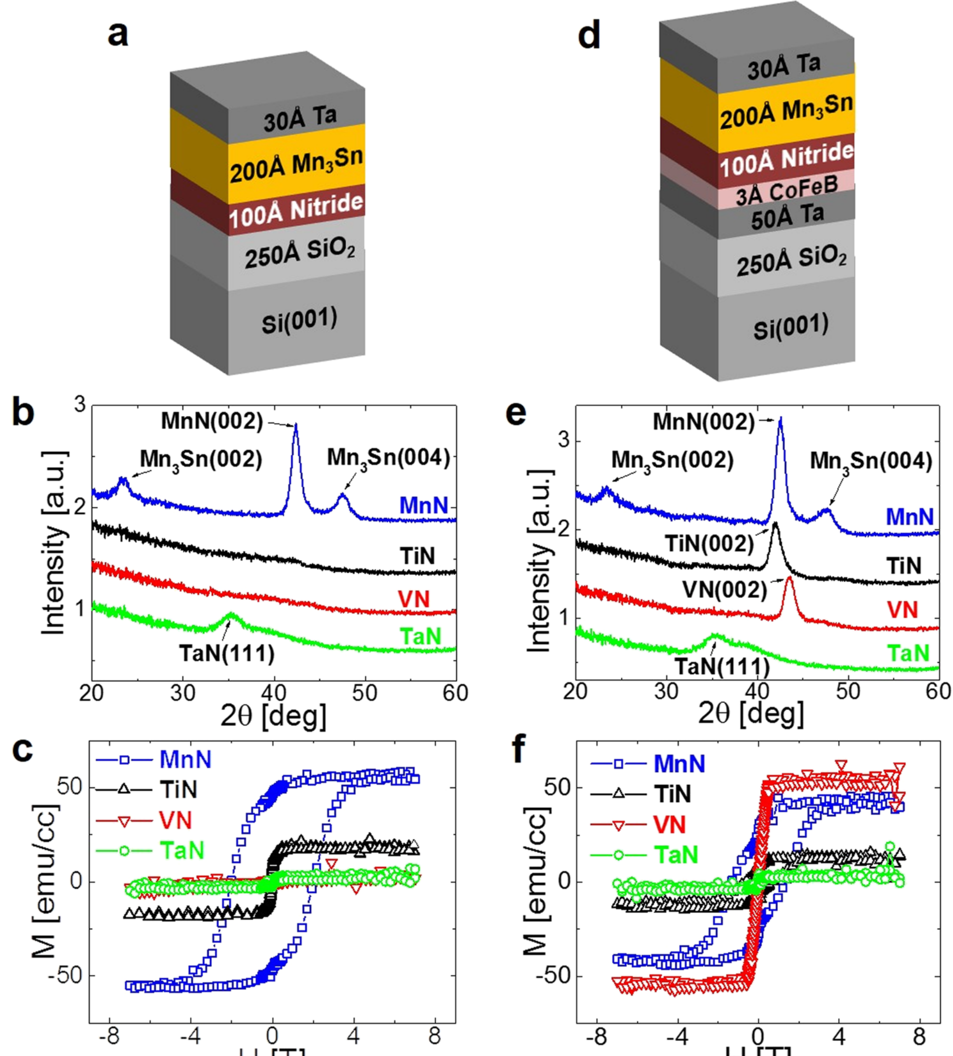

FIG. 3. [(a) and (d)] Schematics of the film stacks deposited using Si(001)/SiO_2 substrates, with the nitride underlayers deposited (a) directly onto the amorphous SiO_2 surface and (d) on a 50 Å Ta/3 Å CoFeB oxygen-free bilayer. [(b) and (e)] XRD out-of-plane θ-2θ scans of the corresponding samples [(a) and (d), respectively] with different nitride underlayers. In (e), the Ta/CoFeB bilayer is found to promote (001)-textured TiN and VN underlayers that, on the other hand, show no preferential orientation when deposited directly on the amorphous SiO_2 layer (b). [(c) and (f)] SQUID-VSM magnetization vs. perpendicular applied field hysteresis loops at ambient temperature of the corresponding samples [(a) and (d), respectively] with different nitride underlayers. Note that MnN is the only underlayer, among the nitride compounds studied here, to successfully promote both the tetragonality [(b) and (e)] and PMA [(c) and (f)] in the Mn_3Sn Heusler films.

(note that their in-plane lattice constant is close and within ~5% of a[t-Mn_3Sn])]. On the other hand, the absence of any diffraction peak from the samples with TiN and VN underlayers suggests that these films are likely polycrystalline with very weak texture and, therefore, they do not promote the oriented growth of the Mn_3Sn films. We note that TiN and VN, as well as SiO_2, are thermally stable materials, and consequently no intermixing between these layers is expected upon substrate heating (i.e., during the deposition of Mn_3Sn). This is confirmed by energy-dispersive X-ray spectroscopy (EDX) measurements illustrated in Figs. S6(a) and S6(b) of the supplementary material. The RS-TaN underlayer film [Fig. 3(b)] displays a (111) orientation, i.e., a three-fold symmetry that does not match the one of tetragonal Mn_3Sn (four-fold symmetry). Hence, not surprisingly, only the MnN/Mn_3Sn sample shows very large PMA stemming from *volume* magnetrocrystalline anisotropy with high coercive fields of ~2 T [Fig. 3(c)]. We note that the magnetization of this Mn_3Sn film is lower than its predicted bulk value (~160 emu/cc) likely due to atomic disorder within the Heusler film. However, we cannot rule out the presence of a small fraction of Mn_3Sn with a different structural phase (e.g., cubic or hexagonal) having lower remanent moment. The samples with TiN, VN, and TaN underlayers show low (and in-plane, for the TiN sample) or negligible (for the VN and TaN samples) moment due to the lack of atomic ordering and orientation of the Heusler layers which is confirmed by HR-TEM images included in Figs. S7 and S8 of the supplementary material.

Remarkably, on a 50 Å Ta/3 Å CoFeB amorphous bilayer both the TiN and VN underlayers crystallize with a (001)-oriented RS structure, whereas the RS-TaN film maintains its (111)-orientation [Fig. 3(e)]. From the XRD data, the extracted cubic RS lattice constants of TiN and VN (~4.29 Å and ~4.15 Å, respectively) are in very good agreement with the predicted values from DFT calculations. Although the 50 Å thick Ta layer is amorphous when deposited on SiO_2 [Fig. S9(a) of the supplementary material], the presence of the NM 3 Å thick CoFeB amorphous layer is crucial to promote

© Author(s) 2019

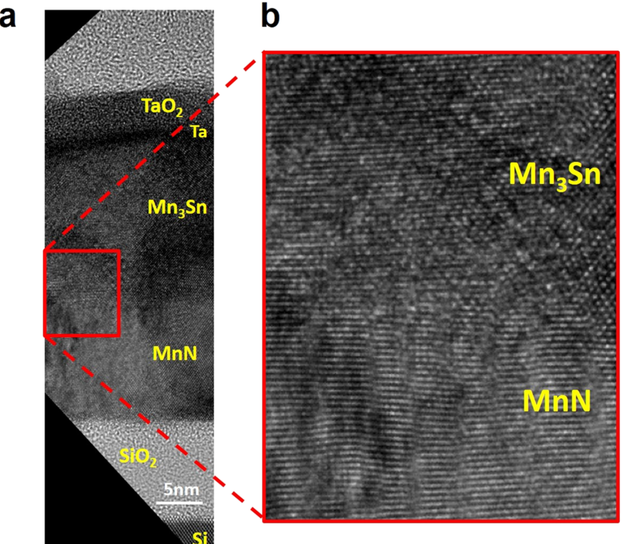

FIG. 4. (a) Cross-sectional HR-TEM image of the sample [having the stack illustrated in Fig. 3(a)] with a MnN underlayer deposited directly on the amorphous SiO_2 surface. The Ta capping film partly oxidizes forming an amorphous TaO_2 layer at its surface. The bright amorphous material above TaO_2 corresponds to the epoxy used during sample preparation. The wavy nature of the Mn_3Sn film surface (r_{rms} ~ 7 Å) is likely due to the substrate temperature of 200 °C used during the deposition of the Heusler layer. This temperature, although modest, can significantly increase films surface roughness.[11] However, we believe that the film surface roughness can be readily improved by adjusting the deposition parameters (e.g., deposition pressure, substrate temperature, magnetron source power) as well as by decreasing the Heusler layer thickness. (b) Zoomed-in view of the MnN/Mn_3Sn interface area in (a) highlighted in red.

preferential (001) orientation of the TiN and VN films. A similar TiN film deposited directly on a 50 Å Ta underlayer without using a 3 Å CoFeB film, displays both (111) and (002) orientations (Fig. S10 of the supplementary material). This is a likely consequence of the formation of a thin TaN layer at the interface between Ta and TiN due to the presence of N_2 within the sputtering plasma. Moreover, HR-TEM images indicate that both TiN and VN underlayers (Figs. S7 and S8 of the supplementary material, respectively) chemically react with the SiO_2 layer forming a rough interface in contrast to the extremely smooth SiO_2/MnN interface [Fig. 4(a)]. A typical pristine SiO_2 surface is very smooth with r_{rms} of <~2 Å. The rough SiO_2/TiN (or VN) interface likely enhances the formation of grains with multiple orientations and leads to very weak texture for these nitride underlayers. Consequently, the Mn_3Sn Heusler layers are polycrystalline without a preferential orientation (Figs. S7 and S8 of the supplementary material) and with no PMA [Fig. 3(c)].

Based on our theoretical calculations, the lattice mismatch between RS-TiN (a = 4.25 Å) and RS-VN (a = 4.12 Å) with t-Mn_3Sn (a = 3.93 Å) is smaller (7.5% and 4.6%, respectively) than between ZB-MnN (a = 4.30 Å) and t-Mn_3Sn (8.6%). Nonetheless, the Mn_3Sn Heusler films deposited on RS-TiN and RS-VN underlayers on a Ta/CoFeB bilayer are polycrystalline [Fig. S9(a) of the supplementary material] with no preferential crystallographic orientation [Fig. 3(e)] and with no PMA [we note in Fig. 3(f) that the sample with a VN underlayer shows a hard-axis hysteresis loop and the one with a TiN underlayer has only a small remanent moment]. On the other hand, (001)-oriented tetragonal Mn_3Sn films [Fig. 3(e)] display PMA also when deposited on a ZB-MnN underlayer using a Ta/CoFeB bilayer [Fig. 3(f)]. These findings validate our theoretical predictions that the stable energy configuration of a t-Mn_3Sn Heusler occurs when this film is deposited on a ZB-MnN underlayer and not on a RS-TiN or RS-VN underlayer. This stability is likely due to the formation of a "continuous" layered structure at the interface between the Mn_3Sn and the ZB-MnN films sharing a common Mn-Mn layer [Fig. 1(b)], which does not occur for any of the other RS-XN underlayers [Fig. 1(a)]. The HR-TEM image of Fig. 4(b) shows, indeed, that the interface between the MnN and Mn_3Sn layers cannot be easily distinguished. Moreover, the presence of alternating atomic planes along the direction perpendicular to the films plane proves the strong (001) texture of both the MnN and Mn_3Sn films.

In summary, we show that metallic films of stoichiometric MnN can readily be deposited by reactive magnetron sputtering by finely tuning the Ar/N_2 ratio during deposition. MnN thin films are experimentally found, for the first time, to crystallize in a cubic zinc-blende structure and to have an AFM configuration, as predicted by our theoretical calculations and by other groups' previous reports. We demonstrate that zinc-blende MnN underlayers allow for the growth of highly (001) textured thin layers of a ferrimagnetic tetragonal binary Heusler compound, Mn_3Sn, that displays strong perpendicular magnetic anisotropy on amorphous substrates. We reason this is likely due to the sharing of an "equivalent" Mn-Mn layer at the interface between ZB-MnN and Mn_3Sn. Despite their smaller lattice mismatch with Mn_3Sn (compared to ZB-MnN), other well-known rock-salt binary nitrides that we investigate (namely, TiN, VN, and TaN) are instead ineffective in promoting the growth of (001) textured Mn_3Sn Heusler films with PMA, in agreement with our density functional theory predictions.

See supplementary material for additional experimental and theoretical calculation details, figures, and methods.

We thank Andrew Kellock for his help with the RBS measurements and analyses, and Erik Lara, Eugene Delania, and Phil Rice for the samples preparation and TEM measurements. Y.F. would like to thank Dr. See-Hun Yang for fruitful discussions. S.F. acknowledges the CNMS User support by the Oak Ridge National Laboratory Division of Scientific User Facilities. We also would like to kindly thank Elena Faleeva for the preparation of Fig. 1.

REFERENCES

[1] D. Apalkov, B. Dieny, and J. M. Slaughter, Proc. IEEE **104**(10), 1796–1830 (2016).
[2] A. D. Kent and D. C. Worledge, Nat. Nanotechnol. **10**, 187 (2015).
[3] J. Slonczewski, J. Magn. Magn. Mater. **159**, L1–L7 (1996).
[4] L. Berger, Phys. Rev. B **54**, 9353 (1996).
[5] T. Graf, S. S. P. Parkin, and C. Felser, IEEE Trans. Magn. **47**(2), 367–373 (2011).
[6] L. Wollmann, S. Chadov, J. Kübler, and C. Felser, Phys. Rev. B **92**(6), 064417 (2015).
[7] S. V. Faleev, Y. Ferrante, J. Jeong, M. G. Samant, B. Jones, and S. S. P. Parkin, Phys. Rev. Mater. **1**(2), 024402 (2017).
[8] F. Wu, E. P. Sajitha, S. Mizukami, D. Watanabe, T. Miyazaki, H. Naganuma, M. Oogane, and Y. Ando, Appl. Phys. Lett. **96**(4), 042505 (2010).

© Author(s) 2019

[9]H. Kurt, N. Baadji, K. Rode, M. Venkatesan, P. Stamenov, S. Sanvito, and J. M. D. Coey, Appl. Phys. Lett. **101**, 132410 (2012).
[10]A. Sugihara, S. Mizukami, Y. Yamada, K. Koike, and T. Miyazaki, Appl. Phys. Lett. **104**(13), 132404 (2014).
[11]J. Jeong, Y. Ferrante, S. V. Faleev, M. G. Samant, C. Felser, and S. S. P. Parkin, Nat. Commun. **7**, 10276 (2016).
[12]P. C. Filippou, J. Jeong, Y. Ferrante, S.-H. Yang, T. Topuria, M. G. Samant, and S. S. P. Parkin, Nat. Commun. **9**, 4653 (2018).
[13]S. V. Faleev, Y. Ferrante, J. Jeong, M. G. Samant, B. Jones, and S. S. P. Parkin, Phys. Rev. Appl. **7**(3), 034022 (2017).
[14]M. Li, X. Jiang, M. G. Samant, C. Felser, and S. S. P. Parkin, Appl. Phys. Lett. **103**, 032410 (2013).
[15]A. Köhler, I. Knez, D. Ebke, C. Felser, and S. S. P. Parkin, Appl. Phys. Lett. **103**, 162406 (2013).
[16]T. Kubota, Y. Miura, D. Watanabe, S. Mizukami, F. Wu, H. Naganuma, X. Zhang, M. Oogane, M. Shirai, Y. Ando, and T. Miyazaki, Appl. Phys. Express **4**, 043002 (2011), Copyright (c) 2011 The Japan Society of Applied Physics.
[17]H.-M. Hong, Y.-J. Kang, J. Kang, E. C. Lee, Y. H. Kim, and K. J. Chang, Phys. Rev. B **72**(14), 144408 (2005).
[18]M. S. Miao and W. R. L. Lambrecht, Phys. Rev. B **71**(21), 214405 (2005).
[19]M. S. Miao and W. R. L. Lambrecht, Phys. Rev. B **76**(19), 195209 (2007).
[20]K. Suzuki, T. Kaneko, H. Yoshida, Y. Obi, H. Fujimori, and H. Morita, J. Alloys Compd. **306**(1), 66–71 (2000).
[21]H. Yang, H. Al-Brithen, E. Trifan, D. C. Ingram, and A. R. Smith, J. Appl. Phys. **91**(3), 1053–1059 (2002).
[22]M. Meinert, B. Büker, D. Graulich, and M. Dunz, Phys. Rev. B **92**(14), 144408 (2015).
[23]P. H. Mayrhofer, D. Music, and J. M. Schneider, J. Appl. Phys. **100**(9), 094906 (2006).
[24]H. Zhao, M. Lei, X. Chen, and W. Tang, J. Mater. Chem. **16**(45), 4407–4412 (2006).
[25]B. R. Zhao, L. Chen, H. L. Luo, M. D. Jack, and D. P. Mullin, Phys. Rev. B **29**(11), 6198–6202 (1984).
[26]F. Kubel, W. Lengauer, K. Yvon, K. Knorr, and A. Junod, Phys. Rev. B **38**(18), 12908–12912 (1988).
[27]N. S. Gajbhiye and R. S. Ningthoujam, Mater. Res. Bull. **41**(9), 1612–1621 (2006).
[28]A. Janotti, S.-H. Wei, and L. Bellaiche, Appl. Phys. Lett. **82**(5), 766–768 (2003).
[29]K. Suzuki, Y. Yamaguchi, T. Kaneko, H. Yoshida, Y. Obi, H. Fujimori, and H. Morita, J. Phys. Soc. Jpn. **70**(4), 1084–1089 (2001).

© Author(s) 2019